

Low-velocity anisotropic Dirac fermions on the side surface of topological insulators

Chang-Youn Moon, Jinhee Han, Hyungjun Lee, and Hyoung Joon Choi*
Department of Physics and IPAP, Yonsei University, Seoul 120-749, Korea
 (Dated: December 2, 2024)

We report anisotropic Dirac-cone surface bands on a side-surface geometry of the topological insulator Bi_2Se_3 revealed by first-principles density-functional calculations. We find that the electron velocity in the side-surface Dirac cone is anisotropically reduced from that in the (111)-surface Dirac cone, and the velocity is not in parallel with the wave vector \mathbf{k} except for \mathbf{k} in high-symmetry directions. The size of the electron spin depends on the direction of \mathbf{k} due to anisotropic variation of the noncollinearity of the electron state. Low-energy effective Hamiltonian is proposed for side-surface Dirac fermions, and its implications are presented including refractive transport phenomena occurring at the edges of topological insulators where different surfaces meet.

PACS numbers: 71.15.Mb, 73.20.-r, 73.61.Ng, 75.70.Tj

Topological insulators (TIs) are characterized by odd number of Dirac-cone-like surface bands which guarantees robust metallicity against arbitrary perturbations preserving time-reversal symmetry [1, 2], and by the helical spin texture of the surface states which leads to remarkable transport properties such as the absence of backscattering by non-magnetic defects as confirmed by experiments [3–5]. The latter feature reminds us of graphene where charge carriers are also described as massless Dirac fermions, as demonstrated intriguingly by the Klein tunneling [6] where normal incident wave exhibits perfect transmission through any finite potential barrier. A crucial difference is that TI involves real spins whereas graphene does pseudo-spins, so that, for example, one-dimensional wires of TI have maximum magnetoconductance at *half integral* flux quanta due to π Berry phase acquired when circling around the wires [7, 8].

Promising TI materials [9, 10] include series of rhombohedral materials Bi_2Se_3 , Bi_2Te_3 , and Sb_2Te_3 proposed by a recent first-principles calculation [9], with the existence of single Dirac cone on their (111) surfaces indeed confirmed by angle-resolved photoemission spectroscopies [11, 12]. Among them, Bi_2Se_3 is considered most promising in the application point of view due to its relatively large bulk band gap of ~ 300 meV that can evade bulk conduction of thermally excited charge carriers at room temperature. This material has a layered structure where the Bi_2Se_3 quintuple layers (QLs) are stacked along the rhombohedral (111) direction [13] combined by van der Waals type interaction. Thus, a natural cleaving face is the (111) surface between two QLs, and it has been the only surface considered theoretically or experimentally so far [14].

Surfaces other than the (111) surface, and interfaces between different surfaces, appear inevitably as step edges on cleaved (111) surfaces [4, 5, 15] and as side surfaces in nanowires or nanoribbons [16–19]. According to the topological band theory [1, 2], a strong TI like Bi_2Se_3 [9] should have odd number of Dirac cones on any arbitrary surface. However, existence of Dirac cones on

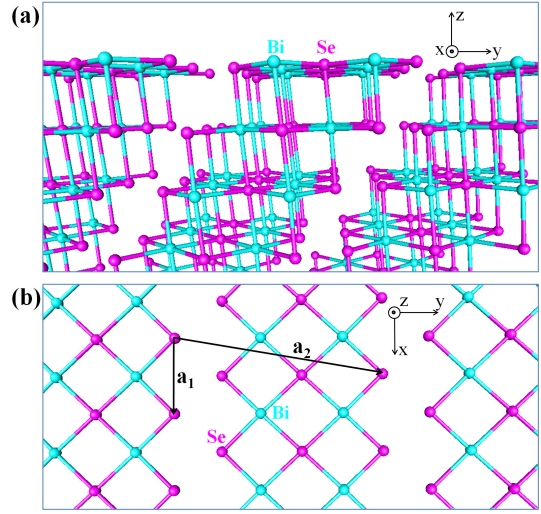


FIG. 1: (Color online). Atomic structure of the Bi_2Se_3 (221) surface. (a) Side view with perspective, showing slanted QLs. (b) Top view of the topmost atomic layer, with surface unit vectors denoted by \mathbf{a}_1 and \mathbf{a}_2 . Using the experimental bulk structure [13], the length of \mathbf{a}_1 is 4.14 Å, the y -component of \mathbf{a}_2 is 11.26 Å long, and the QLs are slanted by 58° .

a surface other than the (111) surface and their physical properties have never been studied by realistic electronic-structure calculations or by direct measurements.

In this Letter, we investigate the electronic structure of a side surface of Bi_2Se_3 using first-principles density-functional calculations, and find a Dirac-cone band structure, for the first time on a surface other than the (111) surface, consistently with the Z_2 topological band theory. We find that the side-surface Dirac cone has lower symmetry, with elliptic equi-energy contour lines, and smaller velocity, introducing the refractive index in analogy with optics. We also present the low-energy Hamiltonian for the side-surface Dirac cone, and reflection and transmission properties at interfaces between different surfaces.

Our first-principles calculations are based on the density-functional theory with the generalized gradient

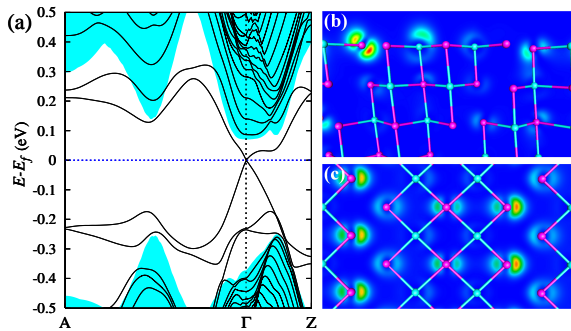


FIG. 2: (Color online). Electronic structure of the Bi_2Se_3 (221) surface. (a) Calculated side-surface electronic band structure from the BZ center to BZ boundaries along the two reciprocal lattice vectors. Filled regions denote bulk continuum states projected on the surface BZ. (b) Side view and (c) top view of a wavefunction at the Dirac point, which show that the state is localized near the surface.

approximation [20] and *ab-initio* norm-conserving pseudopotentials as implemented in SIESTA code [21]. We employ partial-core correction for Bi and Se pseudopotentials, pseudo-atomic orbitals (double- ζ -polarization basis set) for electronic wavefunctions, and a cutoff energy of 500 Ry for real-space mesh. We use a supercell containing a slab of Bi_2Se_3 and 9 Å thick vacuum to study surface states while preventing interaction between periodic images. Brillouin-zone (BZ) integration is performed with a two-dimensional (2D) 12×6 k -point grid. Spin-orbit interaction is treated by relativistic pseudopotentials in the fully nonlocal form [22]. Atomic positions are taken from the experimental bulk structure [13].

Figure 1 shows the atomic structure of the side surface considered in our present work. This side surface is stoichiometric in the sense that the topmost atomic layer of the surface and other atomic layers in parallel with it have stoichiometric Bi and Se compositions for Bi_2Se_3 within each atomic layer. The normal direction of the side surface is (221) in Miller indices of the rhombohedral bulk structure, making an angle of 58° to the (111) plane. In Fig. 1, no bond is drawn between Se atoms belonging to different QLs to represent the (111) cleaving planes with real-space gaps which are along the x direction and repeated in the y direction. The (221) surface has lower symmetry than the (111) surface, exhibiting anisotropy between x and y directions clearly. We construct a slab of eleven atomic layers of Bi_2Se_3 with the slab thickness of ~ 30 Å to study surface electronic structures.

Figure 2(a) shows calculated electronic band structure along two lines in 2D BZ: from Γ to A and from Γ to Y . Here, A and Y are BZ boundaries along the reciprocal lattice vectors \mathbf{b}_1 and \mathbf{b}_2 , respectively, associated with the real-space unit vectors \mathbf{a}_1 and \mathbf{a}_2 shown in Fig. 1(b). In Fig. 2(a), a crossing of linear bands is clearly visible at the Γ point with the Dirac-point energy coinciding with the Fermi energy (E_f). The bulk band continuum is pro-

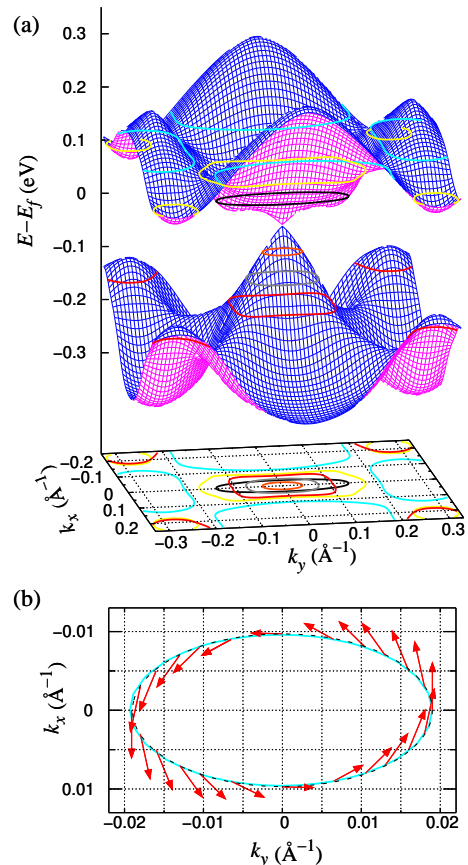


FIG. 3: (Color online). The Dirac cone on the Bi_2Se_3 (221) surface. (a) Calculated 2D electronic band structure near the Dirac point at $\mathbf{k} = 0$. Equi-energy contours for -150, -100, -50, 50, 100, and 150 meV from the Dirac point are drawn on the energy surface and then projected onto the bottom plane. (b) Equi-energy contour at 20 meV below the Dirac point. Arrows denote calculated spins of the states at each \mathbf{k} .

jected onto the 2D surface BZ as filled areas in Fig. 2(a), where the bulk band gap is about 300 meV, consistently with previous calculation [9]. To check if the crossing bands are indeed surface states, we plot the squared amplitude of the wavefunction, $|\psi(\mathbf{r})|^2$, for a state at the Γ point in Figs. 2(b) and (c). We find that it is mainly located on the surface atoms and decays rapidly into the bulk region, showing the surface-state nature of the crossing bands. Around the Γ point in Fig. 2(a), we notice that the slope of the linear band is steeper, i.e. the Fermi velocity is larger, along the Γ - A direction than Γ - Y , indicating anisotropy of the Dirac cone. Particle-hole asymmetry is also visible, where band linearity persists down to ~ 200 meV below E_f while the two bands bend significantly only ~ 30 meV above E_f .

The shape of the side-surface Dirac cone is more obvious in the 2D plot of the bands near the Γ point, as shown in Fig. 3(a). The Dirac cone is anisotropic, with the slope of the band and hence the Fermi velocity being larger in the x direction than in the y direction. As mentioned

above, the linear band feature holds only within a very small energy window near E_f , so the energy contours of 50 meV above E_f (in black) and below E_f (in orange) look very different from each other [Fig. 3(a)]. At energies near E_f close enough to ensure the band linearity, the energy contours are basically very close to ellipses.

We obtain the spin of a Dirac-cone state on the (221) surface by evaluating expectation values of the three spin-operator components, and the results are shown in Fig. 3(b). As expected for the helical spin fermion, the spin is almost perpendicular to the wave vector \mathbf{k} . Meanwhile, since each electronic state in this material is not a spin eigenstate but a noncollinear spin state due to the spin-orbit interaction, the spin size is not necessarily $1 \mu_B$ in general [23]. Unlike the (111) surface where the spin size is independent of \mathbf{k} , the spin size in the (221)-surface Dirac cone is found to depend on \mathbf{k} , having its maximal value of $0.83 \mu_B$ at $k_x = 0$ and gradually decreasing toward $0.55 \mu_B$ at $k_y = 0$ around the Dirac cone [Fig. 3(b)].

Now we consider low-energy effective Hamiltonian similar to the previously suggested one [9] which basically corresponds to a Rashba-type surface spin-orbit Hamiltonian. Considering the reduced symmetry, the (221)-surface Hamiltonian in the first order of k would be

$$H = \hbar(-v_x \sigma_y k_x + v_y \sigma_x k_y), \quad (1)$$

where σ_x and σ_y are the Pauli matrices. The Fermi velocities v_x and v_y in x and y directions on the (221) surface are 3.1×10^5 m/s and 1.4×10^5 m/s, respectively, from our first-principles calculations. Energy eigenvalues are

$$E = \pm \hbar \sqrt{v_x^2 k_x^2 + v_y^2 k_y^2}, \quad (2)$$

and the corresponding eigenstates are

$$\psi_{\mathbf{k}}(\mathbf{r}) = \frac{e^{i\mathbf{k}\cdot\mathbf{r}}}{\sqrt{2}} \begin{pmatrix} 1 \\ \pm(-iv_x k_x + v_y k_y) / \sqrt{v_x^2 k_x^2 + v_y^2 k_y^2} \end{pmatrix}. \quad (3)$$

In Eqs. (2) and (3), the plus sign is for the conduction band while the minus sign is for the valence band. The equi-energy contour from Eq. (2) is an ellipse, which agrees with Fig. 3(b) at $E = -20$ meV.

As mentioned earlier, interfaces of different surfaces are very often involved in many experimental situations where two different surfaces meet as a form of step edges on a cleaved TI surface or geometric edges in TI nanowires and nanoribbons. As our result shows that different TI surfaces have Dirac cones with different velocities, we can expect reflection and refraction behaviors in electronic transports at the interfaces of TI surfaces in close analogy with optics with distinct refractive-index materials. The concept of the refractive index can be introduced to a TI surface, and it provides a new insight for electronic transport in various TI geometries. We discuss two basic cases, a simple interface of TI surfaces and a Fabry-Perot interferometer.

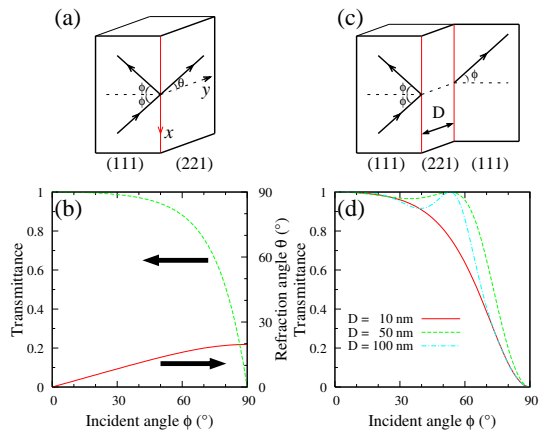


FIG. 4: (Color online). Ray optics of Dirac fermions in TI. (a) Schematic diagram of the edge of the (111) and (221) surfaces in Bi_2Se_3 . (b) Transmission probability T and transmission angle θ as functions of incident angle ϕ in (b). (c) Schematic diagram of the Fabry-Perot interferometer consisting of (111)/(221)/(111) surfaces. (d) T as a function of ϕ with the (221)-surface widths of 10, 50, and 100 nm in (c).

First we consider a simple interface between (111) and (221) surfaces which is parallel to the x direction [Fig. 4(a)]. When a Dirac-cone state of the wave vector \mathbf{k} is incident from the (111) surface to the interface at $y = 0$, with the incident angle ϕ , we can obtain the transmission probability T and the refraction angle θ from the equality of x -components of incident, reflected, and transmitted wave vectors, the energy conservation, and the continuity of the wave functions at the interface, similarly to the graphene case previously studied [6, 24, 25]:

$$T = \frac{\cos(\phi - \theta') + \cos(\phi + \theta')}{1 + \cos(\phi + \theta')}, \quad (4)$$

where $\theta' \equiv \tan^{-1}(v_x k_x / v_y q_y)$ appears from the relative phase of the two spinor components in Eq. (3). The refraction angle θ is given by $\theta = \tan^{-1}(k_x / q_y)$, where $k_x = k \sin \phi$ and $q_y = \sqrt{v_0^2 k^2 - v_x^2 k_x^2} / v_y$ is the y -component of the wave vector in the (221) surface region. The Fermi velocity v_0 in the (111) surface is about 5×10^5 m/s in our calculation, consistently with previous work [9]. Here we note that the incident and refraction angles satisfy the Snell's law with the refractive index n of the TI surfaces defined as the inverse of the phase velocity ($v_{ph} = E / \hbar k$) of Dirac fermions, which, in general, depends on the \mathbf{k} direction but not on the size of \mathbf{k} .

Calculated transmission probability T and refraction angle θ are plotted in Fig. 4(b) as functions of incident angle ϕ at $E = 20$ meV. At normal incidence ($\phi = 0$), T is 1, which means a perfect transmission, demonstrating the absence of back scattering due to the spin texture. As ϕ increases to 90° , T slowly decreases to 0, being greater than 0.5 for ϕ less than 80° . At the same time, the transmission angle θ increases slowly from 0° and reaches

20° at $\phi = 90^\circ$. Thus, in the opposite situation in which the Dirac fermion is incident from the side surface to the (111) surface, the refraction angle reaches 90° already at the incident angle of 20° and at larger incident angles the Dirac fermion cannot transmit through the interface. This implies that *the total internal reflection* can occur when the electron is incident from the side surface to the (111) surface, similarly to the optical system where the incident wave resides in a dielectric with higher refractive index than the other side of the interface. This opens a chance to produce evanescent waves of Dirac fermions on the (111) surface and their related phenomena.

Another relevant geometry is a Fabry-Perot interferometer where the (221) surface is made between two (111) surfaces [Fig. 4(c)], which might be a possible candidate to describe the step edges on the (111) surface in many previous experiments [4, 5]. With boundary conditions similar to the above interface problem, we obtain reflectivity r and hence the reflectance $R = |r|^2$ in analogy with the graphene case [6]

$$R = \frac{\sin^2(q_y D)(\sin\phi - \sin\theta')^2}{\cos^2\phi \cos^2\theta' + \sin^2(q_y D)(\sin\phi - \sin\theta')^2}, \quad (5)$$

where D is the width of the (221) surface region [Fig. 4(c)], and the other parameters are defined similarly to the simple-interface case above.

The transmission probability through the interferometer, $T = 1 - R$, is plotted as a function of the incident angle ϕ in Fig. 4(d), considering three different side-surface widths $D = 10, 50, \text{ and } 100 \text{ nm}$, with $E = 20 \text{ meV}$. For all cases, we have the perfect transmission for the normal incidence ($\phi = 0$) as in the simple-interface case, because of the forbidden back scattering. We also expect a perfect transmission to occur resonantly when the destructive interference happens between the incident and reflected waves, i.e., $q_y D = n\pi$ for positive integer n from Eq. (5). Because of relatively low Fermi velocity in the side surface region, $D = 10 \text{ nm}$ is not large enough for the resonant transmission to occur at $E = 20 \text{ meV}$, so T monotonically decreases from 1 to 0 with increasing ϕ . For larger widths, 50 and 100 nm, T reaches 1 at $\phi = 53^\circ$, where the resonance condition is fulfilled. In the case of $D = 100 \text{ nm}$, the resonance at $\phi = 53^\circ$ is narrower, with less transmission at ϕ between 0° and 53° .

Our Fabry-Perot structure can also be considered as an electronic analogy of the ‘optical fiber’ where propagating waves are confined within the high refractive index (low Fermi velocity) region by the total internal reflection. If the side surface region is clean enough to prevent the waves from escaping into the (111) surface region with high incident angles by defect scattering, this structure might be used as a one-dimensional conducting wire.

In conclusion, we performed first-principles calculations to investigate the electronic structure of a side surface of topological insulator Bi_2Se_3 , finding a Dirac cone

on the side surface, consistently with the topological-band-theory argument. The side-surface Dirac cone is found to be slow and anisotropic in an elliptic shape, with the spin size dependent on \mathbf{k} . The low-energy effective Hamiltonian is proposed for the side-surface Dirac fermions, and the concept of the refractive index is introduced to the TI surface. Refraction, reflection, and transmission behaviors of Dirac fermions are demonstrated in the simple TI interface and the Fabry-Perot TI interferometer. Our idea of making TI junctions using different surfaces can be applied to form more complex structures such as superlattices, opening a chance for novel physical properties of Dirac fermions.

We acknowledge helpful discussions with Jung Hoon Han and Young-Woo Son. This work was supported by NRF of Korea (Grant No. 2009-0081204) and KISTI Supercomputing Center (Project No. KSC-2008-S02-0004).

* Email: h.j.choi@yonsei.ac.kr

- [1] L. Fu, C. L. Kane, and E. J. Mele, Phys. Rev. Lett. **98**, 106803 (2007).
- [2] J. E. Moore and L. Balents, Phys. Rev. B **75**, 121306 (2007).
- [3] P. Roushan *et al.*, Nature (London) **460**, 1106 (2009).
- [4] T. Zhang *et al.*, Phys. Rev. Lett. **103**, 266803 (2009).
- [5] Z. Alpichshev *et al.*, Phys. Rev. Lett. **104**, 016401 (2010).
- [6] M. I. Katsnelson, K. S. Novoselov, and A. K. Geim, Nature Phys. **2**, 620 (2006).
- [7] J. H. Bardarson, P. W. Brouwer, and J. E. Moore, Phys. Rev. Lett. **105**, 156803 (2010).
- [8] Y. Zhang and A. Vishwanath, Phys. Rev. Lett. **105**, 206601 (2010).
- [9] H. Zhang *et al.*, Nature Phys. **5**, 438 (2009).
- [10] H. Lin *et al.*, Nature Mater. **9**, 546 (2010); H. Lin *et al.*, Phys. Rev. Lett. **105**, 036404 (2010).
- [11] Y. Xia *et al.*, Nature Phys. **5**, 398 (2009).
- [12] D. Hsieh *et al.*, Phys. Rev. Lett. **103**, 146401 (2009).
- [13] R. W. G. Wyckoff, *Crystal Structures*, Vol. 2. (John Wiley and Sons, New York, 1964).
- [14] J.-H. Song, H. Jin, and A. J. Freeman, Phys. Rev. Lett. **105**, 096403 (2010).
- [15] J. Seo *et al.*, Nature (London) **466**, 343 (2010).
- [16] D. Kong *et al.*, Nano Lett. **10**, 329 (2010).
- [17] J. J. Cha *et al.*, Nano Lett. **10**, 1076 (2010).
- [18] S. S. Hong *et al.*, Nano Lett. **10**, 3118 (2010).
- [19] H. Peng *et al.*, Nature Mater. **9**, 225 (2010).
- [20] J. P. Perdew, K. Burke, and M. Ernzerhof, Phys. Rev. Lett. **77**, 3865 (1996).
- [21] D. Sanchez-Portal, P. Ordejon, E. Artacho, and J. M. Soler, Int. J. Quantum Chem. **65**, 453 (1997).
- [22] L. Kleinman and D. M. Bylander, Phys. Rev. Lett. **48**, 1425 (1982).
- [23] C. L. Kane and E. J. Mele, Phys. Rev. Lett. **95**, 146802 (2005); O. V. Yazyev, J. E. Moore, and S. G. Louie, *ibid.* **105**, 266806 (2010).
- [24] A. H. Castro Neto *et al.*, Rev. Mod. Phys. **81**, 109 (2009).
- [25] C.-H. Park *et al.*, Nano Lett. **8**, 2920 (2008).